Supplementary Information

Regulating Spin Order of Transition Metal Embedded-MXenes for Boosting Electrocatalytic Nitrogen Reduction to Ammonia

Neng Li,[a,b*] Zheng Wang,[a,b] Peng Zhang,[c] Xin Li,[d] Arramel Arramel,[e] Chenghua Sun,[f] Xing Zhou,[g] Xiujian Zhao[a]

[a]*State Key Laboratory of Silicate Materials for Architectures, Wuhan University of Technology, Wuhan 430070, China. E-mail: lineng@whut.edu.cn*
[b]*Shenzhen Research Institute of Wuhan University of Technology, Shenzhen 518000, Guangdong, China.*

[c]*State Center for International Cooperation on Designer Low-Carbon & Environmental Materials (CDLCEM), School of Materials Science and Engineering, Zhengzhou University, Zhengzhou 450001, Henan, China.*
[d]*Institute of Biomass Engineering, Key Laboratory of Energy Plants Resource and Utilization, Ministry of Agriculture and Rural Affairs, South China Agricultural University, Guangzhou 510642, China*
[e]*Nano Center Indonesia, Jalan Raya PUSPIPTEK, South Tangerang, Banten 15314, Indonesia*
[f]*Department of Chemistry and Biotechnology, Faculty of Science, Engineering & Technology, Swinburne University of Technology, Hawthorn, Victoria 3122, Australia*
[f]*Faculty of Printing, Packaging Engineering and Digital Media Technology, Xi'an University of Technology, Xi'an, China*

Supplementary Notes

From the capture of nitrogen by the catalyst to the production of ammonia is a process involving six electrons. As shown in **Supplementary Fig. 1**, the eNRR has three mechanisms: distal, alternating, and enzymatic, which differ according to the location chosen for protonation in each step. In both the distal and alternate mechanisms, nitrogen adsorbs to the catalytic site in a vertical conformation. The difference between the two mechanisms is that in the distal mechanism, the three protons attack the distal nitrogen atom continuously and do not attack the proximal nitrogen atom until an ammonia gas is produced and desorbed; whereas in the alternating mechanism, the protons attack the two nitrogen atoms alternately and the final desorption of nitrogen gas is continuous. In the enzymatic mechanism, nitrogen is adsorbed in the catalytic site in a horizontal configuration, while the protonation process is similar to the alternating mechanism, in which protons attack two nitrogen atoms alternately, and finally, the two ammonia gases are taken off in succession. In this work, the eNRR response potentials under the three mechanisms are fully considered.

When the Mo_2CS_2 surface is loaded with a double atom, it is possible to specify the initial spin orientation of the metal atom by setting the positive or negative MAGMOM. It was calculated that Mo_2CS_2 surface loaded with two Fe was able to fix the spin direction of both Fe in the same or opposite direction throughout the catalytic process. Moreover, when no nitrogen molecules are adsorbed, the energy of two iron atoms with the same spin direction is 0.29 eV smaller than that with opposite spins. When two Ni are loaded on the surface of Mo_2CS_2, the magnetic moment of the two nickel atoms is zero and cannot be regulated by setting the value of MAGMOM. In contrary, when the Mo_2CS_2 surface is loaded with Fe and Ni, the spin directions of Fe and Ni will eventually be opposite after optimization to a stable structure even if the initial values of the spin directions of both atoms are specified to be the same. The magnetic changes of Fe sites during NRR are shown in **Supplementary Table 6**.

For the double atoms anchored on the MXene surface, the loading sites of these two atoms were determined by comparing the energies of the different adsorption configurations. As shown in **Supplementary Fig. 9** and **Supplementary Table 2**., for

the three possible loading configurations of hcp-hcp,fcc-fcc and hcp-fcc, the four diatomic catalysts are more stable with both atoms in the hcp site.

The interaction between the two atoms should be considered first when introducing two atoms onto Mo_2CS_2 surfaces. The two-dimensional charge differences of Fe&Fe/Ni&Ni/Fe&Ni are shown in **Supplementary Fig. 4a** from top to bottom, respectively, with red color (blue) corresponding to the loss (gain) charge. Charge transfer occurs mainly between Fe/Ni and the adjacent sulfur atoms rather than between two atoms close to each other. However, the *d*-orbital energy level splitting behavior of two atoms is completely different from that of a single atom. **Supplementary Fig. 4b,c** shows the Fe and Ni *d* orbit PDOS on Fe&Ni@Mo_2CS_2, respectively(other diatomic catalysts Fe and Ni d orbit PDOS are presented in **Supplementary Fig. 5**). We have found that d_{xz}, d_{yz} and d_{xy}, $d_{x^2-y^2}$ degenerate when the Mo_2CS_2 surface is loaded with single atoms. The *d*-orbital of Fe and Ni is split into five completely different energy levels when the Mo_2CS_2 surface is loaded with double atoms. The *d*-orbital splitting behavior of Fe and Ni does not depend on the charge transfer between the two, and we propose decoherence arises between the charge and the contributing orbitals.

By comparing the changes in the magnetic moments of metal atoms before and after the adsorption of nitrogen, (**Supplementary Table 3 & 4** show the d-orbital electron rearrangement of transition metal atoms after adsorption of nitrogen adsorption causes a change in magnetic moment and Bader Charge. **Supplementary Fig. 7 & 8** display the corresponding positions of Fe and Ni atoms as listed in the table), we investigate the delicate rearrangement of *d*-orbital electrons of metal atoms that could facilitate the MXenes magnetic properties. An interesting phenomenon is that two atoms with opposite spin directions exhibit antiferromagnetic and weakly ferromagnetic atoms with *d*-orbital electron rearrangement occurring between the two atoms, and a net spin magnetic moment appears for the nitrogen molecule. The double-site adsorption of nitrogen enables the indirect exchange of electrons from the two neighboring transition metal *d*-orbitals. As shown in **Supplementary Fig. 4d**, Fe&Fe@Mo_2CS_2 diatomic catalyst as an example, the nitrogen molecules in the ground states are non-magnetic and therefore cannot be magnetized spontaneously. Nevertheless, the stacked intersection of nitrogen molecules and iron atom orbitals provides the opportunity to

realize charge transfer between *p*-orbital and *d*-orbital. The *d*-orbital of the spin-down iron atom first accepts an electron from the spin-down *p*-orbital of the nitrogen, and then the free *p*-orbital accepts an electron transferred from the spin-up iron atom, resulting in a net spin magnetic moment for the nitrogen molecule. This proposed mechanism of charge transfer facilitated by nitrogen atoms weakens the nitrogen triple bond and mediates the eNRR.

Computational methods

Spin-polarized density functional theory (DFT) calculations were performed by using the Vienna *ab initio* simulation package (VASP)[1,2]. The generalized gradient approximation (GGA) with the Perdew-Burke-Emzerhof (PBE)[3] functional was utilized to describe the exchange-correlation energy. Projector augmented wave (PAW) methods were employed for the pseudopotentials[4]. The energy cutoff for the plane-wave basis was 450 eV, and the convergence threshold for geometry relaxation was 10^{-5} eV in energy and 0.02 eV $Å^{-1}$ in force. The DFT-D3 method[5] was employed to consider the van der Waals interaction. The k-points in the Brillouin zone were sampled with a 3 × 3 × 1 and 5 × 5 × 1 grid centered for structure optimization and static self-consistent calculations, respectively. Bader charge analysis[6] was applied to investigate the electron transfer between neighboring atoms.

In our simulation study, according to the computational hydrogen electrode (CHE) model proposed by Nørskov and colleagues,[7] the Gibbs free energy change ΔG was used to evaluate the eNRR performance, which was obtained as follows:

$$G(T) = E_{\mathrm{DFT}} + E_{\mathrm{ZPE}} + U(\mathrm{T}) - TS + \Delta G_{\mathrm{pH}}.$$

Here $T = 298.15$ K, E_{DFT} and E_{ZEP} are the energy output from the VASP calculation and the zero-point vibration energy, respectively, and external U and S are the internal energy and entropy of the system, respectively. ΔG_{pH} is the free energy correction value of H^+ which can be determined as

$$\Delta G_{\mathrm{pH}} = k_{\mathrm{B}}T \times \mathrm{pH} \times \ln 10 .$$

The energy, zero-point energy (ZPE) and entropy of hydrogen, nitrogen and ammonia are shown in **Supplementary Table 4.**

On the other hand, based on the lowest energy obtained for the adsorption

configuration, the binding energies (E_b) is calculated by the following equation:

$$E_b = E_{tot} - E_{sub} - E_{ads}.$$

where E_{tot} is the total energy of an adsorbate on the Mo_2CS_2, E_{sub} is the energy of the substrate, and E_{ads} is the energy of the adsorbate species.

Supplementary Tables

Supplementary Table 1 Adsorption energy at different adsorption sites.

Adsorption site	Adsorption Energy (eV)		
	S	Fe	Ni
top	-8.36	-1.37	-2.60
fcc	-10.78	-2.50	-3.85
hcp	-11.81	-2.96	-4.23

Supplementary Table 2 Comparison of adsorption energy of double atoms on Mo_2CS_2 surface with different loading configurations.

Adsorption site	Adsorption Energy (eV)				
	Fe&Ni		Fe(α)&Fe(α)	Fe(α)&Fe(β)	Ni&Ni
hcp-hcp	-7.14		-6.02	-5.84	-8.46
fcc-fcc	-6.22		-5.21	-4.55	-7.38
hcp-fcc	hcp-fcc	-6.58	-5.27	-5.28	-7.87
	fcc-hcp	-6.53			

Supplementary Table 3 Charge transfer and magnetic moment of Fe&Ni@Mo_2CS_2.

Type	Bader Charge(e)				Moment(μ_B)			
Fe	-0.24				2.45			
Ni	+0.02				0			
Fe&Fe	Fe_1(α)	Fe_2(α)	Fe_1(α)	Fe_2(β)	Fe_1(α)	Fe_2(α)	Fe_1(α)	Fe_2(β)
	-0.11	-0.11	-0.09	-0.10	2.22	2.22	2.08	-2.08
Ni&Ni	Ni_1		Ni_2		Ni_1		Ni_2	
	0.06		0.06		0		0	
Fe&Ni	Fe		Ni		Fe		Ni	
	-0.19		+0.08		2.39		0.06	

Supplementary Table 4 Charge transfer and magnetic moment of N_2 adsorption on Fe&Ni@Mo_2CS_2.

Type	Bader Charge								Moment(μ_B)							
	Vertical				Horizontal				Vertical				Horizontal			
Fe	-0.44				-0.42				2.38				0.06			
Ni	-0.14				-0.14				0				0			
Fe&Fe	$Fe_1(\alpha)$	$Fe_2(\alpha)$	$Fe_1(\alpha)$	$Fe_2(\beta)$	$Fe_1(\alpha)$	$Fe_2(\alpha)$	$Fe_1(\alpha)$	$Fe_2(\beta)$	$Fe_1(\alpha)$	$Fe_2(\alpha)$	$Fe_1(\alpha)$	$Fe_2(\beta)$	$Fe_1(\alpha)$	$Fe_2(\alpha)$	$Fe_1(\alpha)$	$Fe_2(\beta)$
	-0.32	-0.21	-0.31	-0.19	-0.33	-0.44	-0.36	-0.43	1.92	2.52	1.45	-2.35	0.21	2.50	1.37	-2.52
Ni&Ni	Ni_1	Ni_2	Ni_1	Ni_2	Ni_1	Ni_2	Ni_1	Ni_2								
	-0.12	+0.03	-0.17	-0.16	0	0	0.18	0.19								
Fe&Ni	Fe	Ni	Fe	Ni	Fe	Ni	Fe	Ni								
	-0.40	+0.04	-0.37	-0.15	2.26	0.17	1.33	-0.09								

Supplementary Table 5 Energy, zero point energy (ZPE) and entropy of small molecules: hydrogen, nitrogen and ammonia.

Molecules	Energy (eV)	E_{ZPE} (eV)	S*T (eV)
H_2	-6.77	0.27	0.40
N_2	-16.63	0.15	0.59
NH_3	-19.54	0.91	0.60

Supplementary Table 6 Magnetic properties of Fe sites during the NRR process.

Type		Moment(μ_B)							
		Slab	N_2	N_2H_1	N_2H_2	N_2H_3	N_2H_4	N_2H_5	Slab
Fe	Distal	2.452	2.381	1.841	0.763	0	0.679	3.008	2.452
	Alternating	2.452	2.381	1.841	2.517	1.77	2.454	3.008	2.452
	Enzymntic	2.452	2.527	1.838	2.372	1.621	2.449	3.008	2.452
Fe&Ni	Distal	2.392	2.264	1.642	0.738	0	0.66	2.898	2.408
	Enzymntic	2.392	1.334	2.702	2.615	0.512	2.422	2.898	2.408
Fe(α)&Fe(α)	Distal(Fe1)	2.224	1.923	0.141	0.894	0.061	2.766	2.831	2.258
	Distal(Fe2)	2.221	2.522	2.377	2.396	2.319	0.609	2.824	2.26
	Enzymntic(Fe1)	2.224	0.214	2.6	2.517	2.65	2.257	2.831	2.258
	Enzymntic(Fe2)	2.221	2.503	1.439	2.517	2.785	2.239	2.824	2.26
Fe(α)&Fe(β)	Alternating(Fe1)	2.081	1.447	0.141	1.395	1.555	1.517	2.521	2.118
	Alternating(Fe2)	-2.083	-2.35	-2.377	-2.302	-2.074	-2.28	-2.414	-2.119
	Enzymntic(Fe1)	2.081	1.369	0.205	2.292	2.144	1.912	2.521	2.118
	Enzymntic(Fe2)	-2.083	-2.515	-1.46	-2.293	-2.71	-1.89	-2.414	-2.119

Supplementary Table 7 Adsorption energy of N_2 and H_2O, H^+ on Fe or Ni surfaces.

Type	Adsorption Energy (eV)			
	N_2(Vertical)	N_2(Horizontal)	H_2O	H^+
Fe	-1.17	-0.71	-0.31	0.99
Ni	-1.01	-0.42	-0.71	0.64
Fe&Ni	-1.21	-0.77	-0.73	-0.49
Fe(α)&Fe(α)	-1.14	-1.29	-0.84	-0.62
Fe(α)&Fe(β)	-1.32	-1.32	-0.85	-0.63
Ni&Ni	-0.96	-0.63	-0.51	-0.08

Supplementary Figures

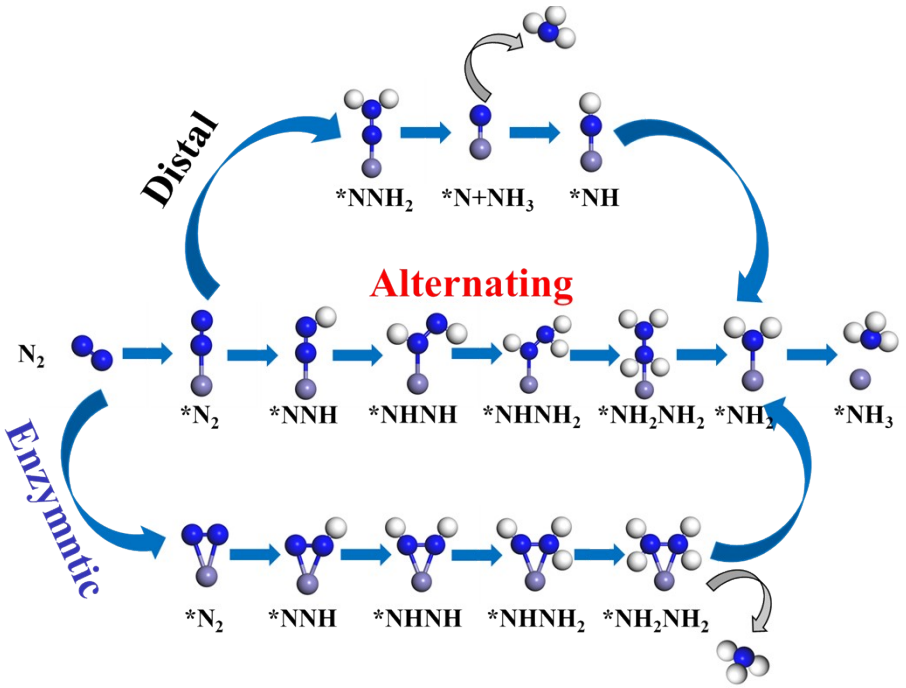

Supplementary Fig. 1 The proposed mechanism on electrocatalytic nitrogen reduction reaction.

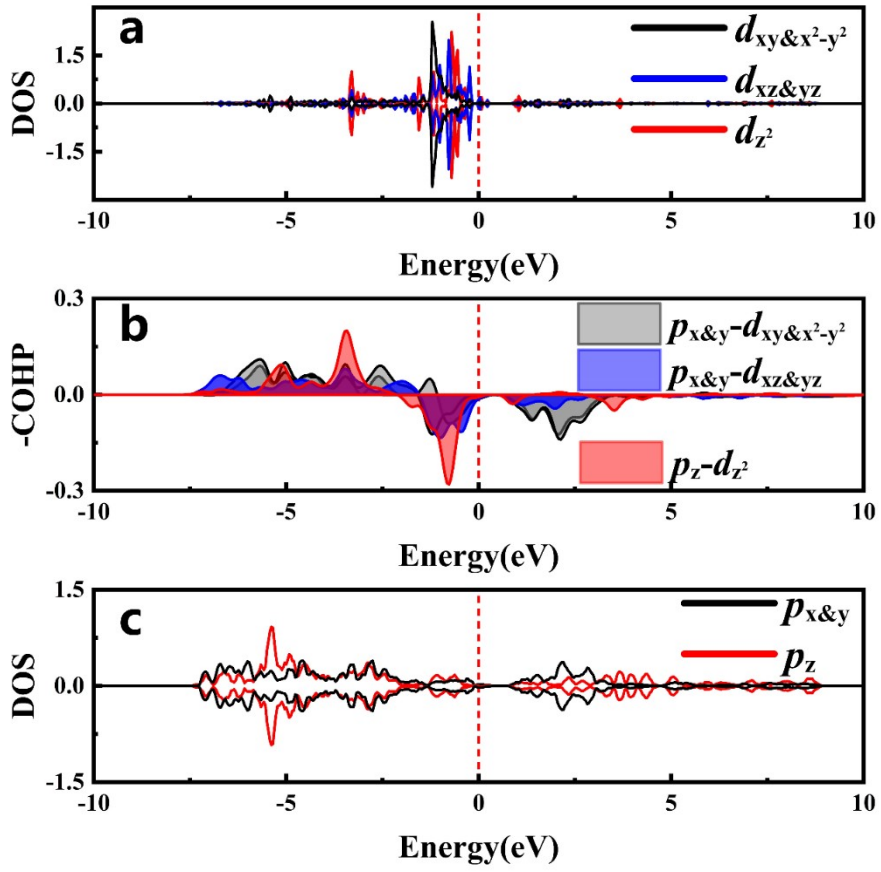

Supplementary Fig. 2 (a) Density of States of Ni atom in Ni@$MoCS_2$, **(b)** Crystal Orbital Hamilton Populations of Ni-S, (**c**) Density of States of S atom in Ni@$MoCS_2$.

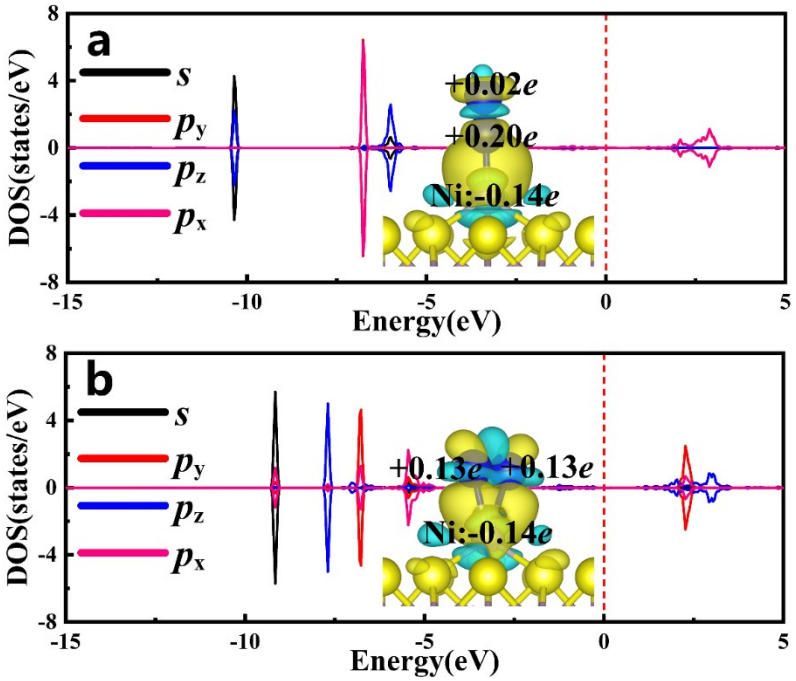

Supplementary Fig. 3 The PDOS and differential charge density of N_2 adsorbed on Ni@Mo_2CS_2.

(a) N_2 vertical adsorption, **(b)** N_2 horizontal adsorption.

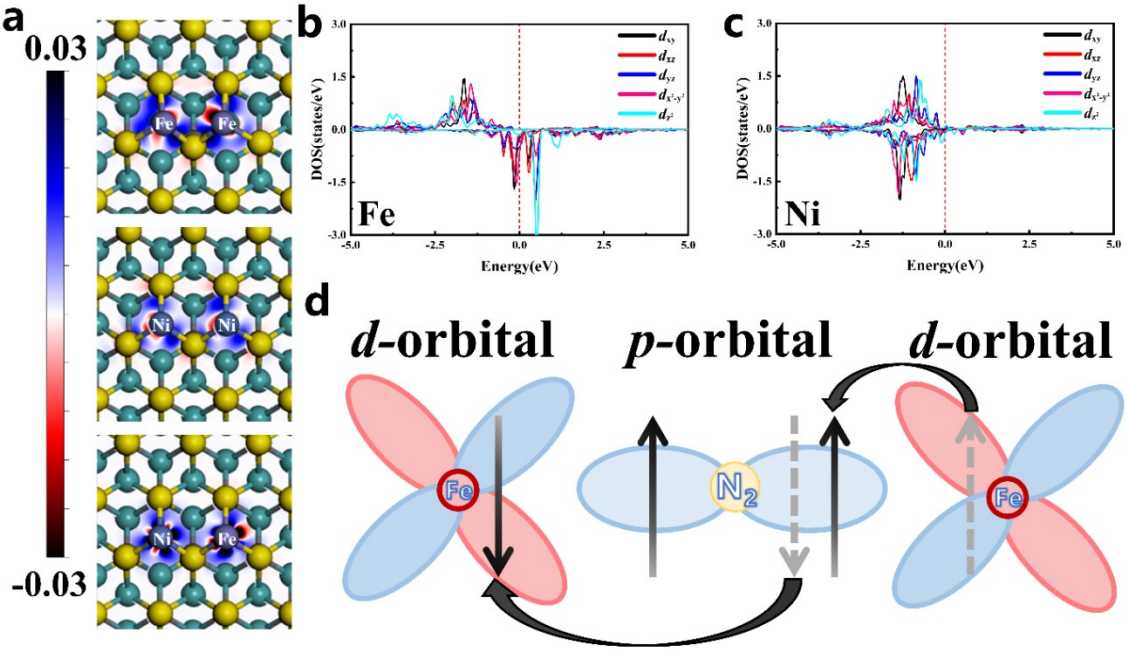

Supplementary Fig. 4. **Charge polarization and *d*-orbital splitting of Fe&Ni@Mo_2CS_2. a** Two-dimensional charge differences between Fe&Fe/Ni&Ni/Fe&Ni and Mo_2CS_2 substrates. **b** Fe and **c** Ni *d*-orbit PDOS on Fe&Ni@Mo_2CS_2 surface. **d** Electron exchange between Fe(α)-N_2-Fe(β) when nitrogen is horizontally adsorbed on the surface of Fe&Fe@Mo_2CS_2.

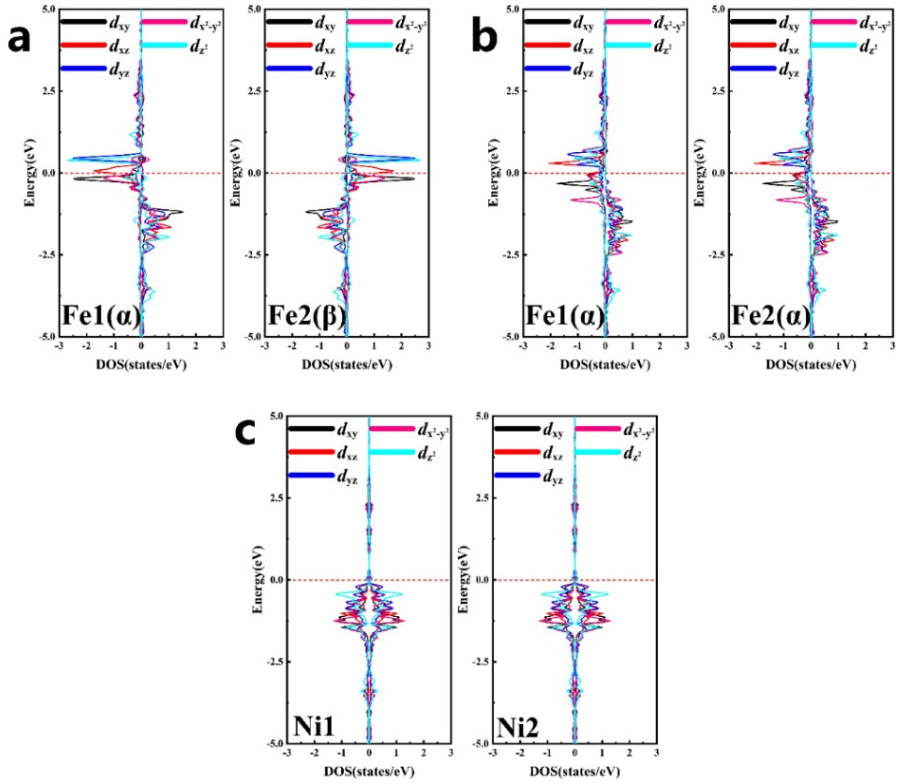

Supplementary Fig. 5 The PDOS of Fe and Ni atom in **(a)** Fe(α)&Fe(β)@Mo_2CS_2, **(b)** Fe(α)&Fe(α)@Mo_2CS_2, **(c)** Ni&Ni@Mo_2CS_2.

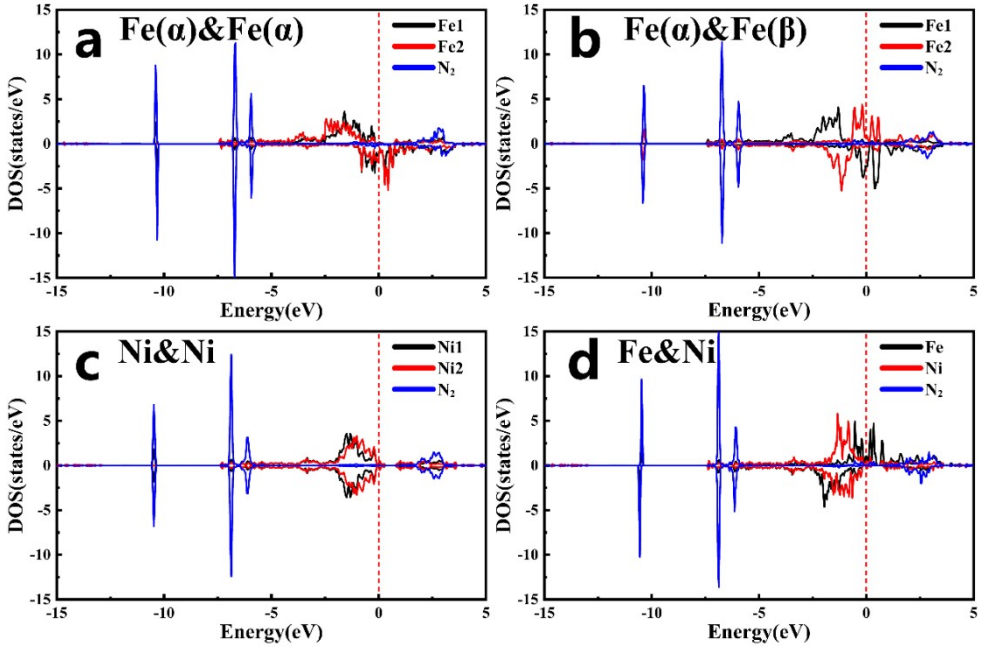

Supplementary Fig. 6 The PDOS of the N_2 adsorbed on Fe & Ni @Mo_2CS_2 with different spin states. **(a)** Fe&Fe-FM state, **(b)** Fe&Fe-AFM state, **(c)** Ni&Ni-NM state, and **(d)** Fe&Ni-FiM state.

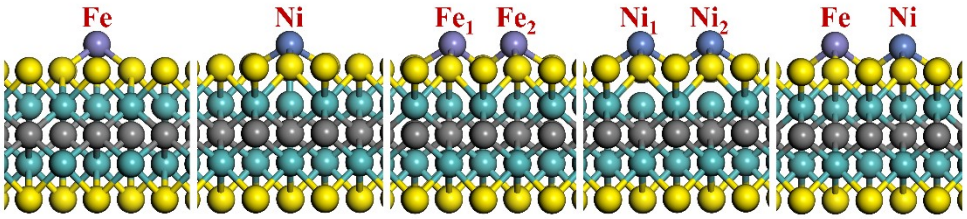

Supplementary Fig. 7 The side view of five different configurations of Fe&Ni@$MoCS_2$.

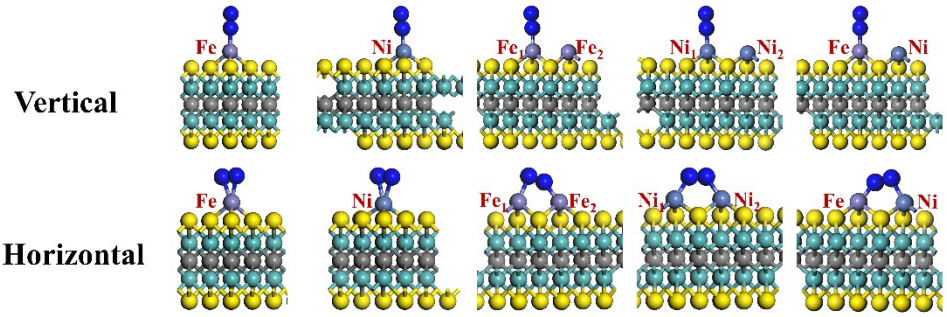

Supplementary Fig. 8 The side view of five different configurations of N_2 adsorbed on the Fe&Ni@$MoCS_2$.

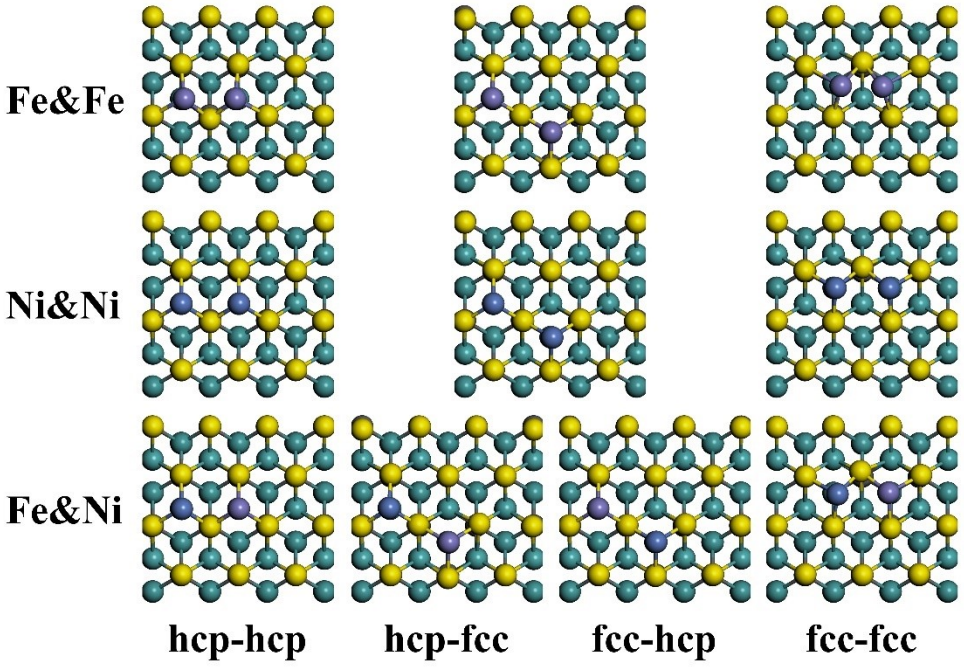

Supplementary Fig. 9 Double atoms on Mo_2CS_2 surface with different loading configurations.

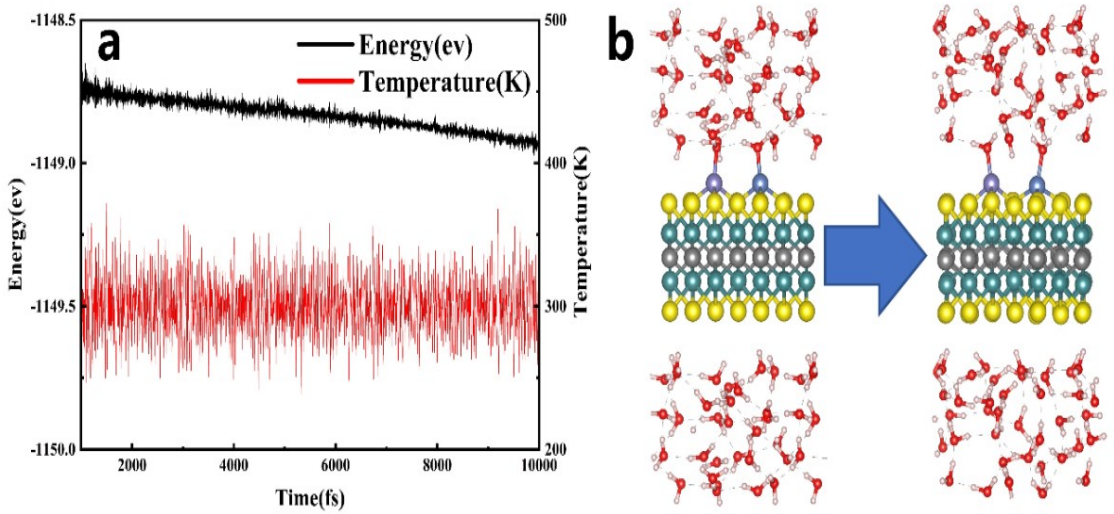

Supplementary Fig. 10 The energy profile of Fe&Ni@Mo_2CS_2 with temperature by AIMD. (a) The energy vibration of energy of the Fe&Ni@Mo_2CS_2 under 300 K with 10000 fs; **(b)** Comparison of the structure of Fe&Ni@Mo_2CS_2 without and with temperature.

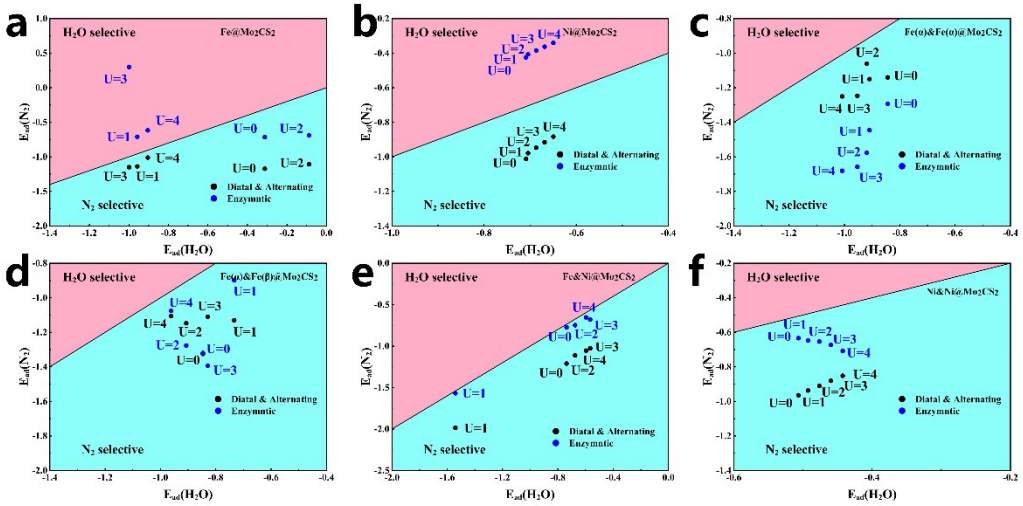

Supplementary Fig. 11 Comparison of adsorption energies of N_2 and H_2O at different U values calculated using the PBE+U method.

References

1. Kresse, G.; Furthmüller, J. Efficiency of Ab-Initio Total Energy Calculations for Metals and Semiconductors Using a Plane-Wave Basis Set. *Comput. Mater. Sci.* **1996**, *6* (1), 15–50. https://doi.org/10.1016/0927-0256(96)00008-0.
2. Kresse, G.; Furthmüller, J.; Hafner, J. Theory of the Crystal Structures of Selenium and Tellurium: The Effect of Generalized-Gradient Corrections to the Local-Density Approximation. *Phys. Rev. B* **1994**, *50* (18), 13181–13185.

https://doi.org/10.1103/PhysRevB.50.13181.

3. Perdew, J. P.; Chevary, J. A.; Vosko, S. H.; Jackson, K. A.; Pederson, M. R.; Singh, D. J.; Fiolhais, C. Atoms, Molecules, Solids, and Surfaces: Applications of the Generalized Gradient Approximation for Exchange and Correlation. *Phys. Rev. B* **1992**, *46* (11), 6671–6687. https://doi.org/10.1103/PhysRevB.46.6671.
4. Blöchl, P. E. Projector Augmented-Wave Method. *Phys. Rev. B* **1994**, *50* (24), 17953–17979. https://doi.org/10.1103/PhysRevB.50.17953.
5. Grimme, S.; Antony, J.; Ehrlich, S.; Krieg, H. A Consistent and Accurate Ab Initio Parametrization of Density Functional Dispersion Correction (DFT-D) for the 94 Elements H-Pu. *J. Chem. Phys.* **2010**, *132* (15), 154104. https://doi.org/10.1063/1.3382344.
6. Tang, W.; Sanville, E.; Henkelman, G. A Grid-Based Bader Analysis Algorithm without Lattice Bias. *J. Phys.: Condens. Matter* **2009**, *21* (8), 084204. https://doi.org/10.1088/0953-8984/21/8/084204.
7. Nørskov, J. K.; Rossmeisl, J.; Logadottir, A.; Lindqvist, L.; Kitchin, J. R.; Bligaard, T.; Jónsson, H. Origin of the Overpotential for Oxygen Reduction at a Fuel-Cell Cathode. *J. Phys. Chem. B* **2004**, *108* (46), 17886–17892. https://doi.org/10.1021/jp047349j